We are IntechOpen,
the world's leading publisher of
Open Access books
Built by scientists, for scientists

4,800
Open access books available

122,000
International authors and editors

135M
Downloads

Our authors are among the

154
Countries delivered to

TOP 1%
most cited scientists

12.2%
Contributors from top 500 universities

BOOK CITATION INDEX
CLARIVATE ANALYTICS
INDEXED

WEB OF SCIENCE™

Selection of our books indexed in the Book Citation Index
in Web of Science™ Core Collection (BKCI)

Interested in publishing with us?
Contact book.department@intechopen.com

Numbers displayed above are based on latest data collected.
For more information visit www.intechopen.com

Correlating Micro-CT Imaging with Quantitative Histology

Tomáš Gregor, Petra Kochová, Lada Eberlová, Lukáš Nedorost, Eva Prosecká, Václav Liška, Hynek Mírka, David Kachlík, Ivan Pirner, Petr Zimmermann, Anna Králíčková, Milena Králíčková and Zbyněk Tonar

Additional information is available at the end of the chapter

1. Introduction

Advanced biomechanical models of biological tissues should be based on statistical morphometry of tissue architecture. A quantitative description of the microscopic properties of real tissue samples is an advantage when devising computer models that are statistically similar to biological tissues in physiological or pathological conditions. The recent development of X-ray microtomography (micro-CT) has introduced resolution similar to that of routine histology. The aim of this chapter is to review and discuss both automatic image processing and interactive, unbiased stereological tools available for micro-CT scans and histological micrographs. We will demonstrate the practical usability of micro-CT in two different types of three-dimensional (3-D) *ex vivo* samples: (i) bone scaffolds used in tissue engineering and (ii) microvascular corrosion casts.

2. Principles of micro-CT

This chapter covers the basic principles of micro-CT. *Ex vivo* specimens are typically placed on a rotating stage between the X-ray source and the microscope objective, which is followed by a detector (Fig. 1). For high resolution imaging, the sample size must be reduced to a minimum. The dimensions should not exceed 500-1000 times the resolution limit required. In large samples, the X-rays must penetrate more material, which results in a lower photon count and increased exposure time.

Certain devices operate with geometrical magnification only, in which the resolution increases with the distance between the sample and the detector. Unfortunately, increased geometrical magnification can result in blurriness, depending on the X-ray source spot size.
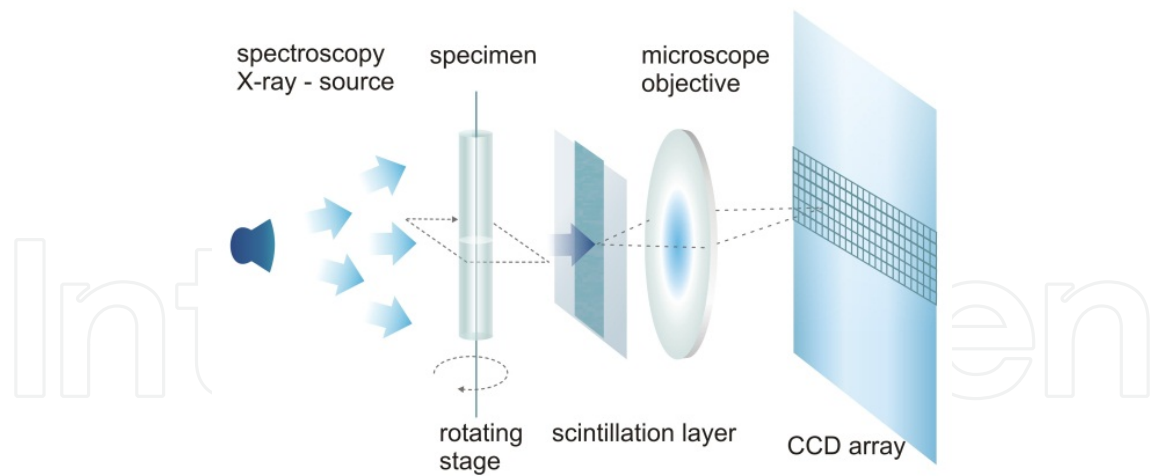
Figure 1. Configuration of a micro-CT scanner with an *ex vivo* sample rotating within a stationary X-ray system (redrawn and modified according to Jorgensen et al., 1998).

More sophisticated devices use microscope objectives for increased magnification and resolution. For optimal settings of the micro-CT scan, the spot size (SS) and the awaited pixel size (PS) are the parameters that set the source distance (SD) and detector distance (DD). When the SD and DD are smaller, higher photon counts can be achieved, thus reducing the time costs. The settings should fulfill equation 1; see also Fig. 2:

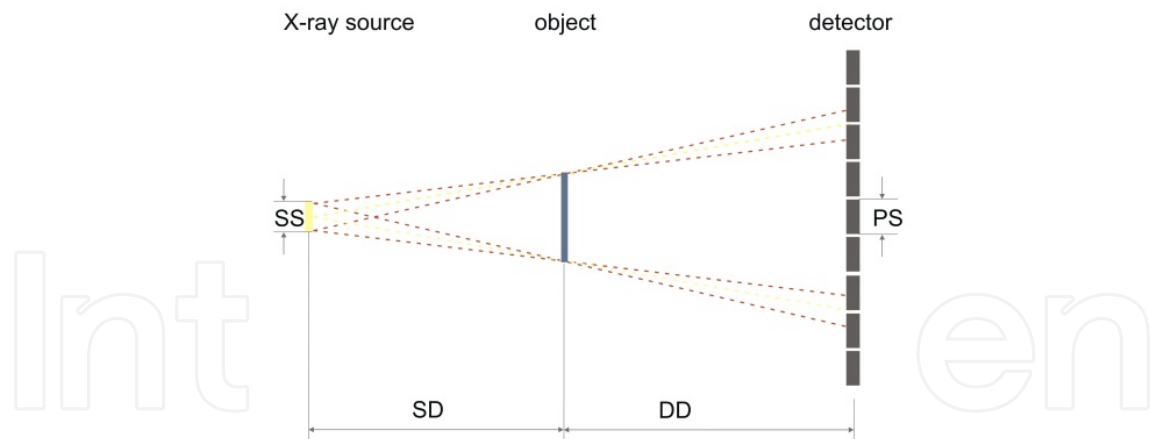$$PS \geq SS \cdot \frac{DD}{SD} \tag{1}$$

Figure 2. For optimal settings of the micro-CT scan, the spot size (SS) and the awaited pixel size (PS) are the parameters that set the source distance (SD) and detector distance (DD) (redrawn and modified according to Roth et al., 2010).

The source SS is strongly dependent on the power of the X-ray tube used. In today's machines, the source SS ranges between 1-10 μm. For high resolution scanning of biological samples, it is advisable to operate with a low accelerating voltage (the typical range for the Xradia XCT 400 (Xradia, Pleasanton, CA, USA) is 20–60 kV used with a power of 4 W, at which the tube yields the lowest SS). The scanning time depends on the magnification and resolution required. For

details smaller than 1 μm, 24 hours or more might be necessary, whereas an overview scan with a pixel size of approximately 10 μm can be achieved within an hour. Sample drifting might be an issue during a long scanning time. From the reconstructed images, the objects of interest are visualized, thresholded, traced and analyzed.

3. Current applications of micro-CT in biomechanics and medicine

Compared with standard human CT devices, which offer a resolution limit of approximately 0.4 mm, the micro-CT introduced a promising modality. However, the clinical use of this method is limited by its higher radiation exposure and longer scanning times. It is used either to visualize individual fine functional and anatomical structures of *ex vivo* human or animal organs (e.g., liver lobules or bone trabeculae) or for whole-body imaging of small animals (Schambach et al., 2010). *In vivo* micro-CT systems are based on a rotating system of X-ray tube and detectors. The construction of these devices is the same as in human CT, except that their dimensions are adapted to small animals (Bag, 2010). The minimal space resolution of *in vivo* micro-CT is from 100 to 30 μm. The imaging of living animals must be faster than in *ex vivo* micro-CT. It is enabled by, among other factors, the use of flat panel detectors that allow us to acquire an abundance of thin sections during one rotation. The examination is also limited by the necessity of using a radiation dose that does not harm the tested animal. In *ex vivo* micro-CT, the X-ray source and the detectors are stationary, and it is possible to adjust the distance between the X-ray tube and the detectors (based on the size of the examined object) to improve the spatial resolution and minimize artifacts. Moreover, in *ex-vivo* micro-CT, time resolution is not important; thus, the examination may take a very long time (hours), and any amount of radiation may be used. This technique enables us to acquire much higher spatial resolution than *in vivo* micro-CT (30 to 1 μm) (Zagorchev et al., 2010).

Most organs have already been analyzed with micro-CT, including bones (Peyrin, 2011), heart and blood vessels (Schambach et al., 2010), lungs, kidney, liver, and cerebral structures (Schambach et al., 2010). Micro-CT devices can be used for the characterization of bone or vascular microarchitecture (Peyrin, 2011; Burghardt et al., 2011; Missbach-Guentner et al., 2011). This method also allows the precise detection of the margins of tumors and their vascularity (Ma et al., 2011; Missbach-Guentner et al., 2011). Tissue composition (e.g., bone mineralization) can be directly linked to 3-D tissue morphometry (Burghardt et al., 2011). Thus, 3-D micro-CT analysis becomes a method of choice for describing the spatial complexity of organ segmentation and the relationships between morphological and functional units (e.g., hepatic lobules and portal acini) (Schladitz, 2011). Micro-CT can also link the imaging of anatomical structures with functional and molecular imaging, e.g., tissue and organ perfusion, the flow rate of exocrine secretions within parenchymatous organs and glands (Marsen et al., 2006), or heart movements (Badea et al., 2005).

For the examination of soft tissues and vessels, contrast solutions are necessary. In *in vivo* imaging, such as in human medicine, standard iodinated contrast media or intravascular blood-pool contrast agents are used (e.g., contrast material covered by a polyethylene glycol

capsule and stabilized by lipoproteins or iodinated triacylglycerides). These blood-pool contrast media are able to remain in the blood circulation for a longer time and thus enable longer scanning times. They do not leave the blood circulation as do standard iodinated contrast agents, which pass into the extravascular interstitial space. Contrast substances labeled with antigens or other ligands (Ritman, 2011) may also be used for targeting and tracking specific structures, such as stem cells (Villa et al., 2010). For *in vivo* studies, nanoparticles can be used to enhance the soft tissue contrast (Boll et al., 2011). It is also possible to use nanoparticles that incorporate into, e.g., tumors and could remain there for longer periods (Boll et al., 2011). However, *ex vivo* micro-CT can utilize any contrast solution, including those that are toxic to living organisms. The only limitation is that they must not damage the examined tissue. In *ex vivo* micro-CT imaging, it is recommended that contrast solutions be used that offer high contrast to the studied tissue, that have a low viscosity to fill the smallest vessels and that do not diffuse out of the blood vessels. In practice, the substances used include silicon rubber (Savai et al., 2009), polymethylmethacrylate with added lead pigment, and gelatin with bismuth or barium sulfate (Zagorchev et al., 2010).

Other modifications of CT applicable in medical experiments are the mini-CT devices (voxel size 10^{-3} mm^3, used for scans of whole organs or small animals) and the nano-CT devices (voxel size of 10^{-7} mm^3) (Ritman, 2011; Müller, 2009).

The greatest progress in micro-CT exploration was acquired in the exploration of tumor microvascularization and the study of neoangiogenesis. The latter phenomenon is also important for the understanding of tumor growth and could be used in oncological treatment strategies, especially in patients treated by biological therapy with antibodies against vascular endothelial factor A (bevacizumab), which inhibits neoangiogenesis (Ma, 2011). Micro-CT imaging of pathological vascularity can provide new information, e.g., about changes in vessel walls in atherosclerosis or other pulmonary vascular diseases (Razavi, 2012).

A promising trend in experimental work is using hybrid methods that combine detailed anatomical information from micro-CT with information about cellular metabolism and structure from methods of nuclear medicine (micro-SPECT/CT and micro-PET/CT) (Ritman, 2011). Therefore, it is appropriate to combine or compare the results of micro-SPECT or micro-PET with, e.g., microscopic analysis of a specimen to estimate the correct anatomical orientation and acquire a satisfactory interpretation of the results. The new suggested tools would be able to use higher energy examination from more X ray sources and thus obtain results on the cellular or subcellular level. The development of new tissue-specific contrast solutions could also be promising for future research activities using micro-CT or its hybrid methods.

4. Micro-CT imaging of biological samples *ex vivo*

4.1. Biomechanics of bone scaffolds

The aim of this chapter is to illustrate the application of micro-CT in tissue engineering and in assessing the biomechanics of biocompatible collagen/hydroxyapatite bone scaffold

samples (Prosecká et al., 2011). Tissue engineering is a promising interdisciplinary research field that aims to develop biological substitutes for the repair of damaged tissue. The typical strategy involves either the delivery of isolated and expanded cell populations within a tissue engineering construct or the recruitment of host cells local to the site of damage through the use of conductive scaffolds and inductive biological signals. The question of how to optimize the design of scaffolds for different tissues remains unsolved. To assess the suitability of polymer tissue scaffolds for use in regenerative medicine, methods to characterize scaffolds are needed (Renghini et al., 2009). The bone scaffolds should be stiff enough to withstand high forces in the bone after implantation but, conversely, should also be flexible enough to enable growth of the cells and changing of the original shape of the graft to meet the needs of the bone complex. Therefore, it is important to perform mechanical measurements and 3-D imaging of bone scaffolds before the seeding of mesenchymal stem cells.

Generally, bones and bone scaffolds can be mechanically tested using various types of techniques: tensile or torsion tests used for strip- or block-shaped tissue specimens; a pressure test used for block-shaped or cylindrical specimens; a ring test in which a ring of given thickness is cut from a tubular organ (typically a blood vessel), clamped into the jaws of special measurement devices and loaded by tension; and an intraluminal pressure inflation-deflation test of tubular organs. The choice depends on the physiological loading of the tissues. The aim is to be as close as possible to the real loading and thus to the real mechanical properties. In any case, regardless of the chosen technique, the result given by a measurement device is of the same nature: a stress-strain (tensile, pressure, ring test) or pressure-outer diameter (inflation-deflation test) curve. The stress-strain curve has a mostly nonlinear shape showing the tissue stiffening as loading increases. The stiffening is caused by various tissue components as they subsequently contribute to the tissue response. The soft component, mostly elastin, contributes to the mechanical response at low loading and is connected with the low stiffness of the tissue, whereas the curly and stiff collagen fibers are straightened as loading progresses and contribute to stiffening at high loading. The relevant portions of a stress-strain curve could be approximated (e.g., by a line), and thus, the mechanical parameters, such as Young's modulus of elasticity at small deformations (low loading) and at large deformations (high loading), the pressure-strain elastic modulus, the initial modulus of compression, the limit stress and the strain in the case of loading until tissue rupture, could be obtained.

To emulate the loading of bones, in which most of their parts are under pressure and only a small fraction of the tissue is under tension, pressure loading was applied to collagen/hydroxyapatite composite bone scaffolds. Cylindrical specimens (approximately 12 mm in diameter and in height) of composite scaffolds containing various amounts of collagen and hydroxyapatite prepared according to Prosecká et al. (2011) underwent pressure mechanical loading with a loading velocity of 1 mm/min. The resultant stress-strain curves, and particularly the regions between 2% and 10% of the original specimen's height, were approximated by linear regression, and thus the initial moduli of compression were determined. (for details of the measurements and their evaluation, see Prosecká et al., 2011).

From a biomechanical point of view, the shape of the stress-strain curves was identical for all compositions of scaffolds. The beginning of each stress-strain curve was linear with low stiffness, and increasing loading led to scaffold stiffening. This stiffening was likely caused by the fact that, with increasing deformation of the porous specimens, the originally high amount of free space filled by air became smaller, and the stiff components became closer together and started to contribute more to the mechanical response. The decreasing porosity caused by the increasing pressure loading could thus be connected with the higher stiffness of the scaffold. The initial modulus of compression increased rapidly with an increase in the collagen concentration. From these two results, we can conclude that not only the composition but also the porosity may play crucial roles in the mechanical properties of collagen/hydroxyapatite composite bone scaffolds.

4.2. Imaging and biological applications of bone scaffolds

The 3-D porous structure and sufficient mechanical stiffness of the bone scaffolds are necessary conditions for the attachment, growth, and progress of mesenchymal osteoprogenitor stem cells (Prosecká et al., 2011); see Fig. 3.
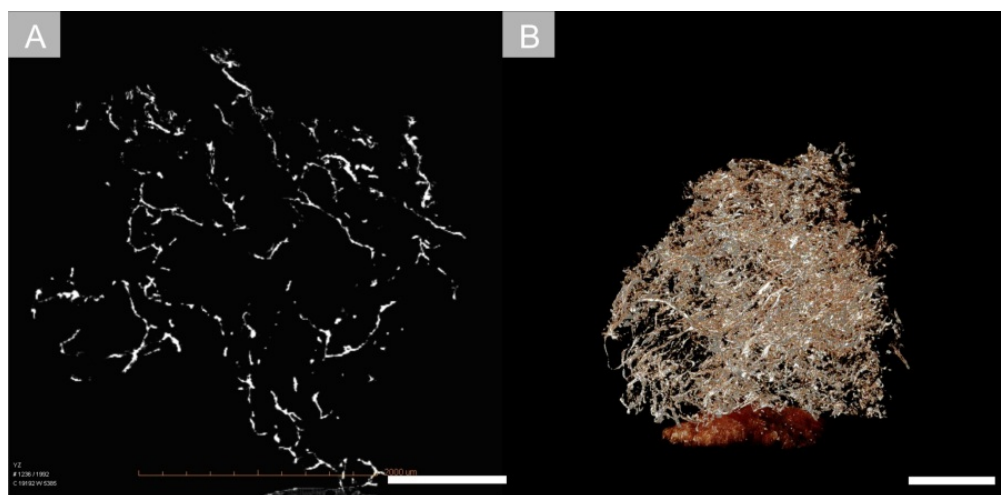

Figure 3. Micro-CT scans of a bone scaffold manufactured from collagen/hydroxyapatite matrix. A – a single section acquired with a 4× objective; the scanning time was 9 hours. B – an image reconstruction based on 3376 sections. The scale bars indicate 1 mm.

Traditional methods for evaluating the osseointegration of tissue-engineered scaffold/cell constructs are based on 2-D histological and radiographic techniques. Sectioning followed by histology can image the scaffold interior but is destructive, lengthy and only semi-quantitative (Ho & Hutmacher, 2006). Fluorescence microscopy can be quantitative when high-throughput approaches are applied, e.g., producing 3-D images with confocal fluorescence microscopy (Tjia & Moghe, 1998). Colorimetric and fluorometric soluble assays are available for cell components, such as enzymes, protein or DNA (Ho & Hutmacher, 2006). However, these soluble assays are quantitative but do not provide information on cell distribution. In contrast to these methods, by micro-CT we can non-destructively obtain 3-D images that penetrate deep into the scaffold interior and produce inherently quantitative

results (Tjia & Moghe, 1998). Micro-CT currently appears to be the most suitable approach for this task (Ho & Hutmacher, 2006; Mather et al., 2007; Mather et al., 2008; Cancedda et al., 2007). Clearly, in a structure as complex as bone, micro-CT provides a distinct advantage over conventional microscopy. Structures can be followed continuously, from the level of osteon to gross bone morphology.

Dorsey et al. (2009) explored the use of X-ray microcomputed tomography for observing cell adhesion and proliferation in polymer scaffolds. The ability of micro-CT to detect cells in scaffolds was compared with those of fluorescence microscopy and a soluble DNA assay. The researchers demonstrated that fluorescence microscopy had better resolution than micro-CT and that the soluble DNA assay was approximately 5 times more sensitive than micro-CT. However, by micro-CT, they were able to reveal the interiors of opaque scaffolds and to obtain quantitative 3-D imaging and analysis via a single, non-invasive modality. They observed that for quantitative micro-CT volume analysis, a cell density of more than 1 million cells/ml is required in the scaffolds. The results demonstrate the benefits and limitations of using micro-CT for the 3-D imaging and analysis of cell adhesion and proliferation in polymer scaffolds. Various bone engineering groups have noted the importance of micro-CT analyses in tissue engineering. Among them, Müller and Rüegsegger have investigated, and quantified, the architecture of cancellous bone using micro-CT (Müller, 1994; Müller et al., 1996, 1998; Rüegsegger, 2001).

In addition to these analyses, a number of morphological measures are being investigated, such as volume fractions of tissues, directivity of calcifying tissue, porosity, pore connectivity, putative vascularization, curvature and surface-to-volume measure (Bentley et al., 2002; Jorgensen et al., 1998).

Despite the advantages of using micro-CT, there are still several issues with both image segmentation and resolution that are exacerbated by the low image contrast due to the low X-ray attenuation of the materials being used (Mather et al., 2008). Morris et al. (2009) studied a method for the generation of computer-simulated scaffolds that resemble foamed polymeric tissue scaffolds. They showed that the quality of the images (and hence the accuracy of any parameters derived from them) may be improved by a combination of pixel binning and by taking multiple images at each angle of rotation. However, micro-CT is considered to be a standard technique in tissue-engineered bones (Cancedda et al., 2007).

5. Three-dimensional imaging of microvascular corrosion casts

5.1. Corrosion casting

Anatomical corrosion casts provide 3-D insights into the arrangement of hollow structures and organ cavities at both the macro- and microscopic levels. The most frequently used are vascular corrosion casts (Giuvărăşteanu, 2007), which, in combination with scanning electron microscopy, constitute the primary application of corrosion casting describing the morphology and anatomical distribution of blood vessels (Lametschwandtner et al., 2004; 2005). Many other examples are found in the literature - the airways (Hojo, 1993), bile ducts

(Gadžijev & Ravnik, 1996), urinary tract (Marques-Sampaio et al., 2007) and lymphatic system (Fujisaka et al., 1996) have been visualized by means of corrosion casting. The steps for obtaining the corrosion casts are as follows: perfusion of the hollow target structures to remove the contents (in the case of vascular casts, prior heparinization is required for the maintenance of blood fluidity), injection of the casting media, its polymerization in the fully filled cavities and the subsequent removal of the surrounding tissues by a highly aggressive corrosive solution. The corrosion casting method has been known since the beginning of the 16th century, when Leonardo da Vinci injected dissolved wax into bovine cerebral chambers (Paluzzi et al., 2007). Over the following centuries, all of the steps in the method have been improved. However, the aim has remained the same – to obtain the most accurate replica of the biological structure.

5.2. Casting media

Because the highest authenticity is required in the proportions of 3-D corrosion casts, casting media must have sufficient viscosity (to pass through but not to penetrate); they must be capable of even, rapid polymerization with minimal shrinkage and of physicochemical resistance to the subsequent corrosion and dissection procedures. All of these properties are combined in methylmethacrylate (MMA) resin. The MMA polymerizing fluid can be produced by warming the MMA monomer with a catalyst, benzoyl peroxide. MMA easily penetrates the capillary network and flows out via the opposite vessels (Kachlík & Hoch, 2008). A polyurethane pigment paste of various colors can be added into the mass along with the X-ray contrast medium, e.g., barium sulfate ($BaSO_4$) or mercury sulfide (HgS) (Gadžijev & Ravnik, 1996). There are also commercially produced, partially polymerized MMAs (e.g., Mercox or Dentacryl), but these products vary considerably in their rheological properties. Dentacryl was used mainly in the last century, originally in dental prosthetics. This compound is a commercially produced, colorless, partially polymerized MMA that is not, due to its high viscosity, suitable for casts of the microvasculature (Kachlík & Hoch, 2008). The greatest advantage of this casting medium is its low cost; thus, Dentacryl is used for more spacious casts, such as those of the bronchial tree (Havránková et al., 1989) or paranasal sinuses (Hajnis, 1988). Painting clays can be used to color Dentacryl. Mercox is a low-viscosity acrylic resin, a MMA monomer stabilized solution. Mercox II (Ladd Research, Williston, Vermont, USA) is commercially offered in two colors (blue and red); the kit contains an MMA resin and a catalyst (benzoyl peroxide). The Mercox II system combines excellent permeability through the entire vascular bed, excellent infiltration properties, short time of preparation and polymerization, minimal shrinkage and high chemical resistance. Although its price is rather high, it is a method of choice for the vascular corrosion casts (Bartel & Lametschwandtner, 2000; Minnich et al., 2002; Lametschwandtner et al., 2004; Kachlik & Baca, 2006, Kachlík & Hoch, 2008).

In our experience with obtaining corrosion casts of porcine liver vascular trees, it is helpful to administer 50,000 IU of heparin in 1 liter of saline and subsequently rinse the vascular bed with 5 liters of Ringer´s solution prior to sacrificing the animal. We found that even the lowest Mercox dilution recommended by the manufacturer (20 ml resin/0.4 g of 40%

benzoylperoxide) polymerizes within a very short time (approximately 5 min), which makes it difficult to fill the complicated liver vasculature (Eberlová, 2012, unpublished results). After 5 minutes of stirring the resin with the catalyst, it was possible to fill a volume of approximately 20 ml before the Mercox started to harden. To prevent any vascular lesions and artifacts, the use of an infusion pump appears to be warranted (Minnich et al., 2002).

Unfortunately, Mercox does not offer sufficient X-ray-opacity for micro-CT. To fill and opacify microvessels *ex vivo*, the silicone rubber Microfil MV (Flow Tech, Inc., Carver, Massachusetts) appears to be a substance of choice (Gössl et al., 2003). The Microfil MV kit is available in five radio-opaque colors and comprises MV-Diluent, MV compound and MV Curing Agent. The working time of Microfil is approximately 20 minutes. However, Microfil MV is not suitable for conventional corrosion casting techniques using potassium hydroxide. Two alternative techniques for the subsequent tissue clearing are offered instead: alcohol-methyl salicylate clearing, which produces a stiffer tissue useful for gross observation, and glycerin clearing, which yields a more flexible tissue and vessels.

6. Automatic image processing, topology analysis and measurement of statistical features

This chapter describes an approach to automatic micro-CT image processing using computer vision techniques and the Mercox vascular corrosion casts of the intestinal mucosa described in the previous chapter. The input data were acquired with Xradia XCT 400 (Xradia, Pleasanton, CA, USA) by scanning Mercox vascular corrosion casts. The resulting data set consisted of a DICOM stack of approximately 1000 slices, each 1000 times 1000 pixels, such that the scanned volume contained 10^9 volume elements (voxels), each represented by a 16-bit signed number. The depicted volume in reality was a cube with an edge of approximately 35 mm, whereas the voxel edge was 36.53 μm. For image processing, we used the Insight Toolkit library for C++ (www.itk.org) and MATLAB with its Image Processing Toolbox (The MathWorks, Inc., Natick, MA, USA). The first step of the image processing was an analysis of the density distribution of the data, using a density histogram; see Fig. 4.

Segmentation is a process in computer vision that divides the voxels of the source image into two subsets – foreground and background – depending on their affinity to the objects of the real world (Sonka et al., 1998). In our case, the foreground was formed by the vascular corrosion cast, whereas all of the other data were considered to be background.

Thresholding is a common and widely used image segmentation method in machine vision. This technique outputs a binary image $g(i,j,k)$ that classifies the voxels of the source image $f(i,j,k)$, in which i, j, k represent the spatial indices of the data, according to equation 2:

$$\begin{aligned} g(i,j,k) &= 1 \quad for\ f(i,j,k) \geq T \\ &= 0 \quad for\ f(i,j,k) < T \end{aligned}$$

(2)

In this equation, *T* is the threshold value; *g(i,j,k)*=1 for image elements of objects and *g(i,j,k)*=0 for image elements of the background (Sonka et al., 1998). The threshold value *32,768*, used for segmentation in our case, is highlighted in red in Fig 4.
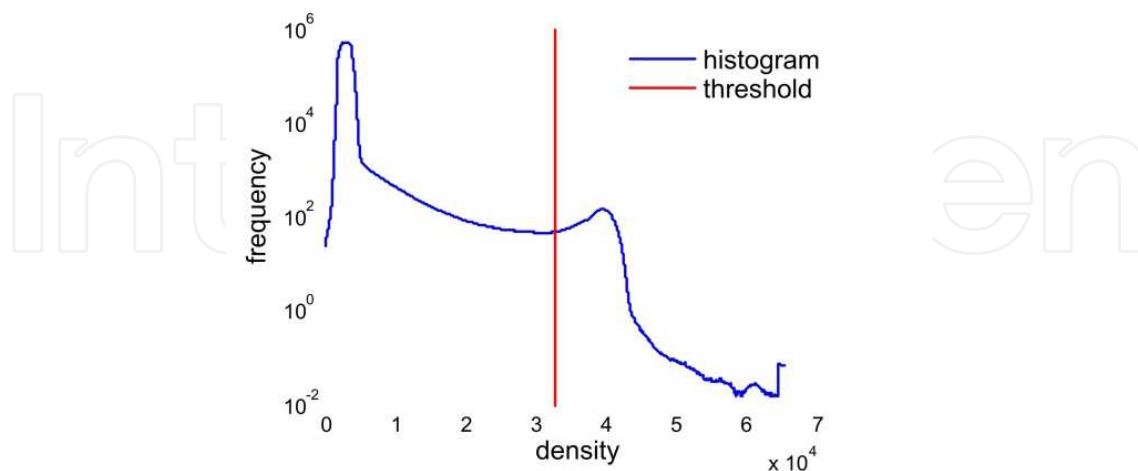

Figure 4. A density histogram of the source image data. In this histogram, which has been smoothened for visualization, we can observe a local minimum prior to a peak representing the density of desired vessel voxels. According to the histogram, the segmentation methods based on density values appear to be suitable for the current image data set.

After segmentation was performed, it was necessary to further pre-process the binary image to eliminate artifacts, e.g., holes and bays caused by irregular spreading of the casting material, and measurement errors. These errors were resolved by applying the morphological operation of hole filling, which converts cavities inside of objects into object voxels. The next step of the data analysis used the labeling algorithm, which assigned a unique label to each contiguous region of a binary image (Sonka et al., 1998). This procedure gave us a large amount of useful information about object counts and sizes in the volume. Part of the label image histogram is shown in Fig. 5.

The label histogram (Fig. 5) demonstrates that there are many objects of insignificant size that are produced simply by measurement noise. We can convert these objects into background and eliminate them from further processing. The size of the objects at which the segmentation of the blood vessel regions becomes unreliable, reveals also the resolution limits of the current micro-CT scan. Acquiring a reliable representation of all of the microvessels would therefore require another scan with a different objective and micro-CT settings. We can also deduct the count of dominant objects in the volume. For the purposes of visualization, in the subsequent processing steps, we will only work with the largest object. Fig. 6 demonstrates the difference between a 3-D model of the whole vessel system (Fig. 6A), and the largest continuous object only (Fig. 6B).

The volumetric image (Fig. 6) is useful for visualization. However, it is not desirable for topological investigation. A shape simplification is needed that would preserve the tree connectivity and geometric conditions. In this study, we used the algorithm introduced by Lee et al. (1994). This algorithm is based on parallel 3-D binary image thinning, which is
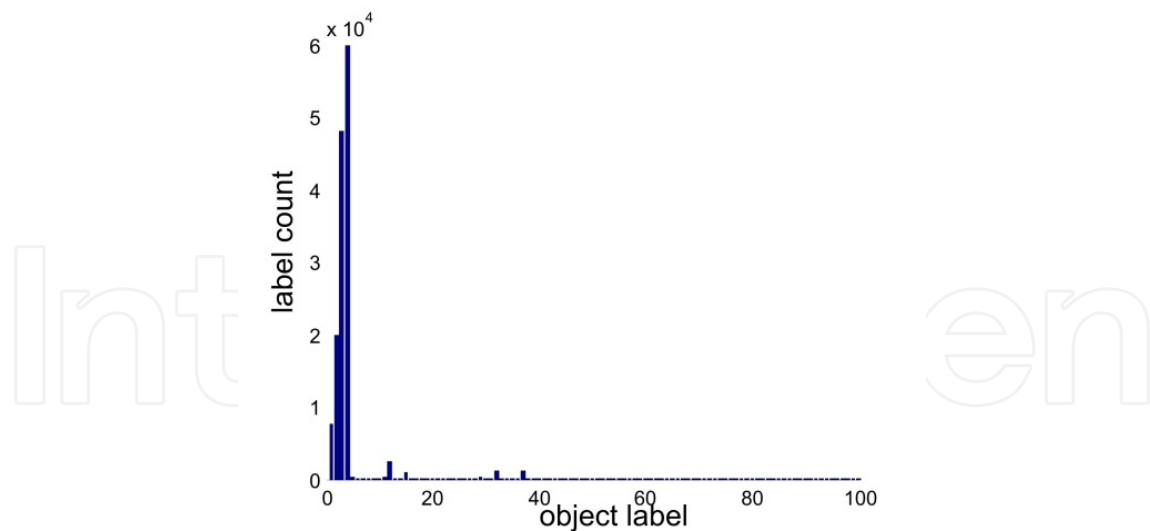
Figure 5. A label image histogram. The object labels each stand for voxels belonging to a single contiguous object, i.e., the count of each label denotes the size of the object it represents, and the number of unique labels corresponds to the number of contiguous objects in the volume. Object labels higher than 100 were omitted for a better overview. There were 1,967 unique objects within the image data set under study.
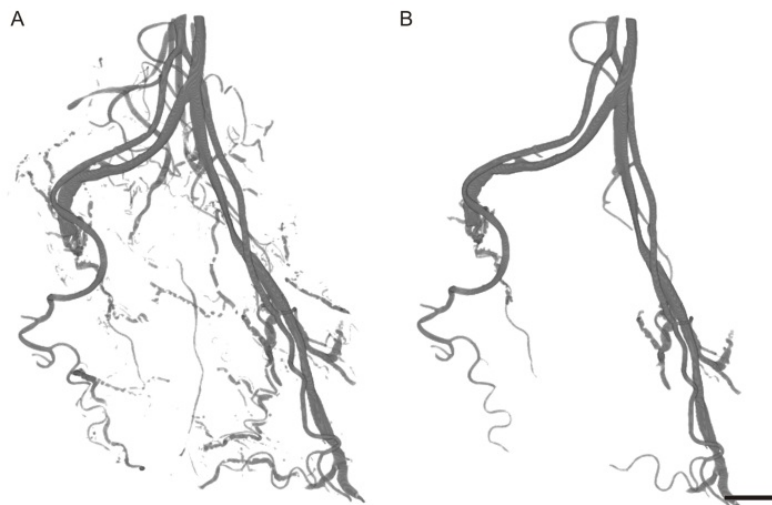

Figure 6. A three-dimensional reconstruction of the entire vessel system (A), and of the largest continuous object (B).

suitable for large data sets and produces a 1-voxel-thin 3-D skeleton. The topology analysis of the skeleton involves identifying the node and terminal points of the tree. The points are located based on their 26-connectivity to neighboring voxels. Based on the properties of the skeletonization algorithm, we can find nodes of valence 3 (i.e., nodes at which three microvascular segments join). Existing nodes of valence 4 are decomposed into two nodes of valence 3. Fig. 7 shows the resulting skeleton with located node points. In this sample, 149 nodes were detected. Using the number of branching points with a known valence, the numerical density of the microvessels $Nv(cap/ref)$ can be estimated, as described by Lokkegaard et al. (2001).

Figure 7. Vessel skeleton with branching node points.

Currently, we are able to segment a vessel tree formed by a corrosive cast. In the example analyzed in this study, continuous regions of the volumetric model were counted to detect the number of individual objects within the volume. The volume of each individual object was estimated. Using skeletonization, the number of branching nodes was counted, and the number of vascular segments between the nodes was estimated, as was the length of each segment. Knowing the vessel length and volume, it is also possible to compute the average diameter of the vessel. However, there are still challenges for future work, such as estimating the vessel diameter in each voxel of the skeleton using a distance transform. With this information, the diameter distribution with respect to the vessel length or the vessel volume could be acquired. With a known diameter, the surface area of the vessels can also be computed. Tracking the skeleton leading its binary graph construction determines the spatial distribution of the branching nodes from the proximal vascular segments to the periphery of the vascular tree.

The approach presented in this chapter is based on several assumptions that deserve to be discussed, as they also represent the limitations of this study. We assume, for our computation, that the vessels are in the form of generalized cylinders, which means that the cross-section orthogonal to the medial axis is a circle. The voxels in our data set were cubical; however, a data set with unequal voxel edges may be resampled into cubical voxels.

An important question is the choice of the threshold value. The segmented vessel diameter is partially linearly dependent on the chosen threshold value. Setting an excessively low threshold causes too many artifacts to appear and objects to merge into each other; contrariwise, an excessively high threshold makes vessels very thin, such that small vessels disappear. This effect implies that the threshold value influences the absolute diameter of the vessels and biases statistical markers. However, the construction of the skeleton and the topological analysis do not appear to be affected by the selection of the threshold.

Let us summarize the advantages and disadvantages of our automatic image processing approach. Compared with stereological methods currently in use (see the next chapter), automatic image processing requires virtually no user interaction. This approach is able to compute the distributions of the volumes, surfaces and lengths of vessels of given diameters with a high precision. Moreover, the stereological methods may be applied to our volumetric model to achieve results comparable to those of stereological measurements performed by a human, but with no interaction at all. A disadvantage is the necessity of the choice of the threshold used for the segmentation, due to the sensitivity of certain results to the threshold settings. As stated before, the threshold value does not greatly influence the topology of the vessel tree but strongly correlates with the diameters of the vessels. A proposed solution to this issue is to compute the skeleton with a higher threshold and the diameters with a lower one.

7. Quantitative micro-CT, histology and stereology

Current micro-CT devices are typically bundled with sophisticated software packages that offer a number of automated quantification procedures. However, correlating the micro-CT results with quantitative histology favors the use of unbiased stereological methods, which are highly standardized and widely accepted in biomedical microscopy research (Howard and Reed, 1998; Mouton, 2002). This chapter illustrates the stereological assessment of micro-CT scans of bone scaffolds and microvascular corrosion casts, including the quantification of the volume fraction (V_V, dimensionless), surface density (S_V, m^{-1}), length density (L_V, m^{-2}), orientation and anisotropy of microvessels (Kochová et al., 2011).

In bone tissue samples, the micro-CT resolution is currently capable of providing images that can be used for both analysis of bone vascular canals, and counting individual osteocyte lacunae. Quantification of bone microporosities is used for testing their effect on the viscoelastic properties of bone tissue (Tonar et al., 2011). The microporosity has at least two functional levels, the vascular porosity (related to the vascular canals; the order of magnitude is 10–1000 µm) and the lacunar-canalicular porosity (surrounding the osteocytes; the order of magnitude is 0.1–10 µm). Mechanical experiments clearly demonstrated that the hierarchical organization of bone architecture is crucial and that bone structural heterogeneity varies with the scale of magnification. Whereas Fig. 8 demonstrates two-dimensional sections of compact bone produced by histology and micro-CT, Fig. 9 shows the results of 3-D micro-CT reconstruction of cancellous bone.

The vascular corrosion casts described in section 4 and used in section 5 also can be assessed with spatial stereological methods. Image data acquired by micro-CT are demonstrated in Fig. 10.

After manually tracing the microvessel profiles within a series of consecutive two-dimensional micro-CT sections (software Ellipse, ViDiTo, Košice, Slovak Republic), a three-dimensional system of oriented lines can be acquired (Fig. 11).
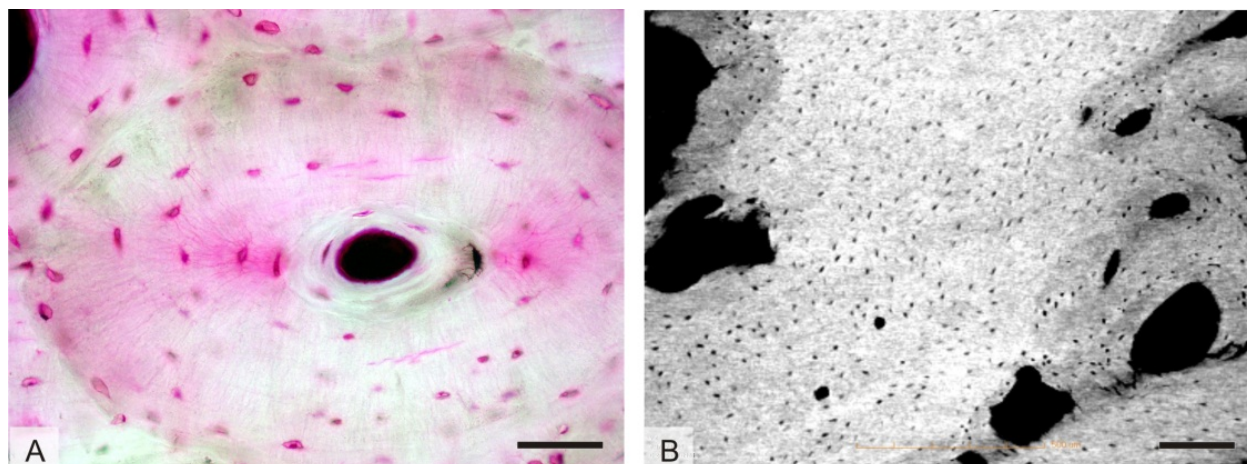
Figure 8. Comparing a histological ground bone section stained with basic fuchsin (A, human femur) with a micro-CT image of compact bone (B, human tibia). In the compact bone, two types of microporosities can be quantified – the osteocyte lacunae and the vascular canals. Both levels of microporosities are clearly visible in either method. The volume fraction of the vascular canals can be quantified stereologically with a point counting method, whereas the numerical density of the osteocyte lacunae can be assessed by the 3-D counting method called disector, which is not biased by the variation in size and orientation of the lacunae (Sterio, 1984; Tonar et al., 2011). The scale bars indicate 60 μm (A) and 200 μm (B).
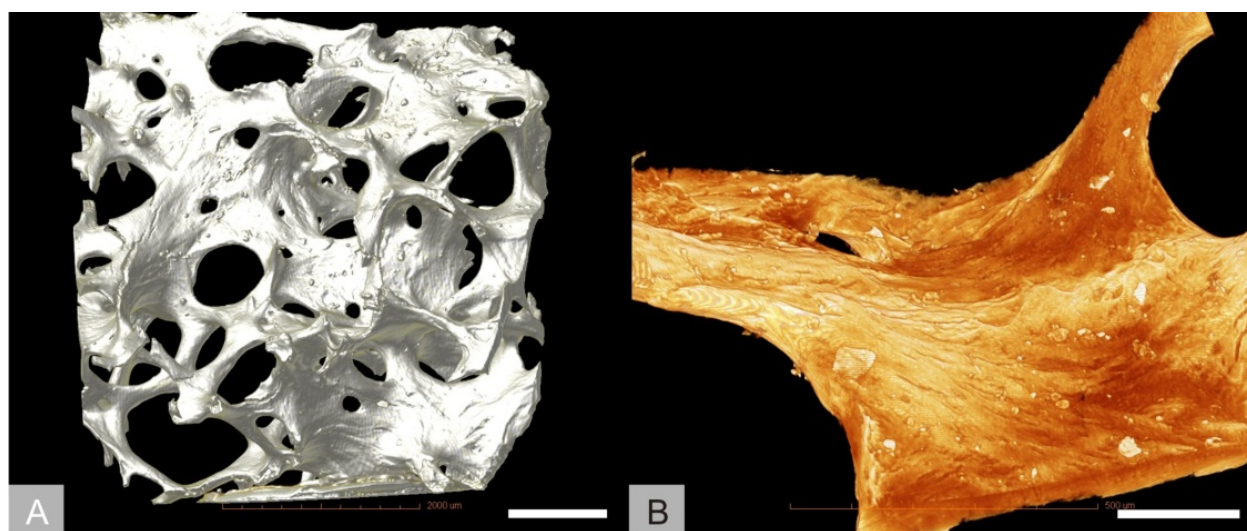
Figure 9. Micro-CT reconstruction of cancellous bone (human tibia) – an overall view (A) and a detail of the surface of bone trabeculae (B). The density and 3-D arrangement of bone trabeculae can be easily assessed with micro-CT. In contrast to scanning electron microscopy of bone surfaces, micro-CT is not biased by perspective or the depth of the 3-D sample. A dry bone sample does not require any laboratory processing prior to micro-CT scanning. The scale bars indicate 1 mm (A) and 200 μm (B).
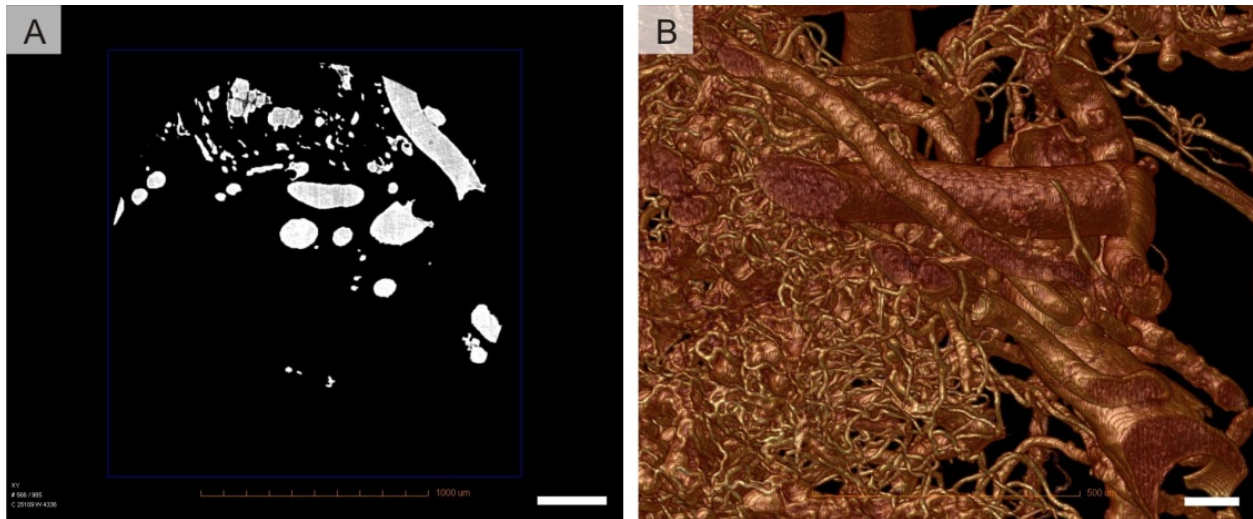
Figure 10. A micro-CT image (A) and a 3-D reconstruction (B) of a vascular corrosion Mercox cast of human intestinal mucosa. The scale bars indicate 300 μm (A) and 100 μm (B).
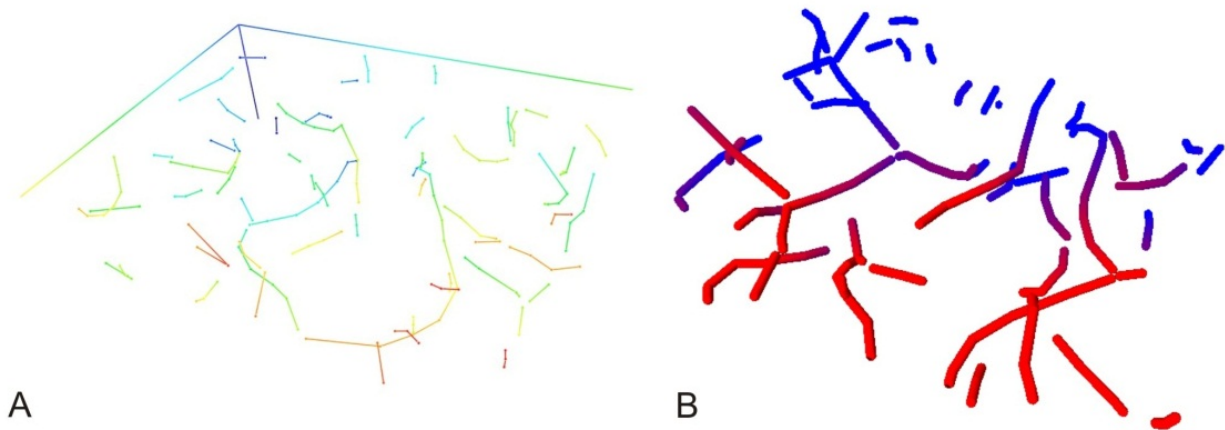

Figure 11. Tracing the microvessel profiles in serial micro-CT sections (Fig. 10A) results in oriented lines, which can be visualized either as linear structures (A) or as rods (B). The blood microvessels are abstracted as having one dimension only (the length), whereas the spatial orientation is retained. The thickness of the rods (B) has been set for better visualization only and does not represent the real thickness of the original microvessels.

Next, the orientation of each skeletonized vessel can be described using a spherical coordinate system (Fig. 12). Each blood vessel segment is described as a vector connecting the center of the coordinate system with the surface of the sphere. This vector is described by its length and a combination of azimuth ranging between $[0, 2\pi]$ and elevation $[0, \pi/2]$.

Next, the combinations of vessel lengths and their 3-D orientation can be assessed using various 2-D plots (Fig. 13). These plots are very useful when assessing the directionality and anisotropy of the vascular segments. Should the anisotropy be quantified, several methods are available, such as the ellipsoidal anisotropy, fractional anisotropy, or a chi-square method comparing the observed length densities of lines with the discrete uniform distribution of an isotropic line system (Kochová et al., 2011).
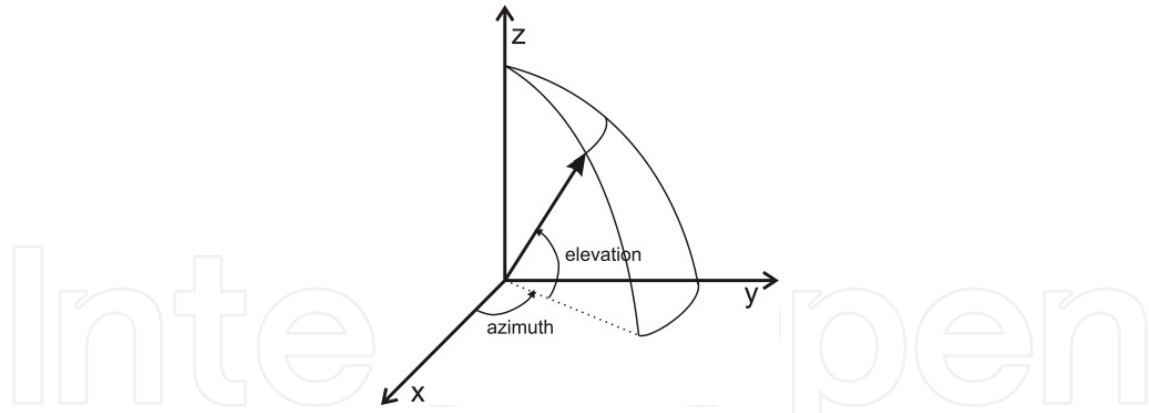
Figure 12. The angular description of the directions of vascular line systems using a spherical coordinate system. Each blood vessel segment is represented by a vector with a known length and a combination of azimuth (longitude) and elevation (latitude). This figure was redrawn and modified according to Kochová et al. (2011).
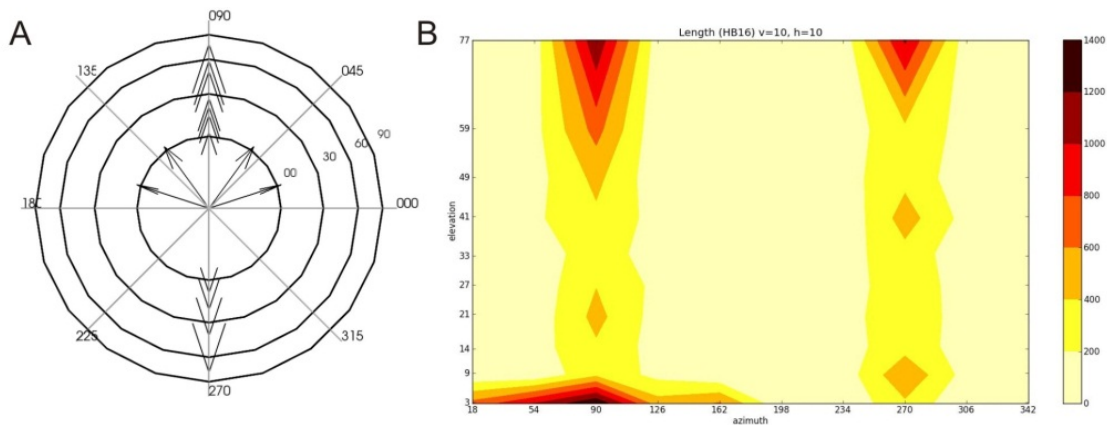

Figure 13. Polar plots can be constructed (A) using the Lambert azimuthal equal area projection. Radial lines are azimuths and concentric lines are elevations, whereas the arrows indicate individual directions. Color histograms can also be used (B) with a color scale corresponding to the microvessel lengths in the given combination of elevation and azimuth (a dark color represents a high value of the microvessel length). In this example, the prevailing directions demonstrate the anisotropy of the microvessels, as both plots exhibit preferential combinations of azimuth and elevation.

Using the skeletons of the microvessels, their lengths L within a reference volume V(ref) can be expressed as the length density Lv; see equation 3:

$$L_V = \frac{L}{V(ref)} .$$ (3)

The volume fraction occupied by the microvascular corrosion cast easily can be estimated using the Cavalieri principle (Howard & Reed, 2005), as shown in equation 4,

$$estV = T \cdot (A_1 + A_2 + ... + A_m),$$ (4)

where *estV* is the estimated volume of the microvessels, *T* is the distance between the sections sampled for the estimation, and *A* is the area of the cast profiles in *m* individual

sections. When estimating the area A, the points hitting the profiles are counted, and their sum is multiplied by the area corresponding to each point. At least 200 points must be counted to obtain a reliable volume estimate (Gundersen & Jensen, 1987); see Fig. 14A.

To simulate the histological measurement of microvessel density Q_A (Fraser et al., 2012), i.e., the number of microvessel profiles Q per area unit A, an unbiased counting frame can be applied (Fig. 14B), and the microvessel density can be expressed using equation 5,
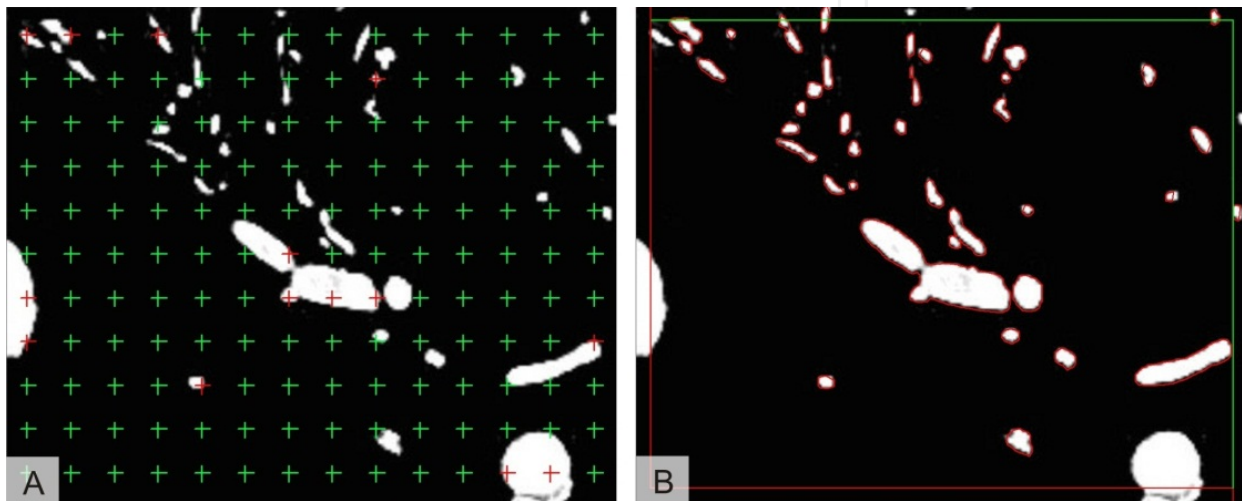
$$Q_A = \frac{Q}{A}. \tag{5}$$

Figure 14. Estimating the volume fraction and the microvessel density. A - When estimating the area and volume of the microvascular cast, the points hitting the profiles (marked red) are counted, and their sum is multiplied by the area corresponding to each point. B – Counting the microvessel profiles per section area simulates the histological assessment of microvessel density. This procedure can be performed using the projection of an unbiased counting frame consisting of two admittance (green) and two forbidden (red) borders. Marked profiles of microvessels (red outlines) situated inside the frame or those touching admittance borders and not touching the forbidden lines are counted in the software Ellipse.

The surfaces of the microvascular casts can also be estimated using stereological methods. However, several of these methods require isotropic uniform random sections or vertical uniform random sections. Randomized orientation of the sections cannot always be guaranteed in micro-CT, as the sample is typically oriented with its long axis perpendicular to the X-ray beam (Fig. 1). The section plane is often arbitrary and cannot be regarded as random. A suitable solution without randomizing the cutting plane is using an isotropic virtual test probe named fakir (Larsen et al., 1998; Kubínová & Janáček, 1998; Kubínová & Janáček, 2001); see Fig. 15. The ratio between the surface area S and the reference volume $V(ref)$ is called the surface density S_V; see equation 6:
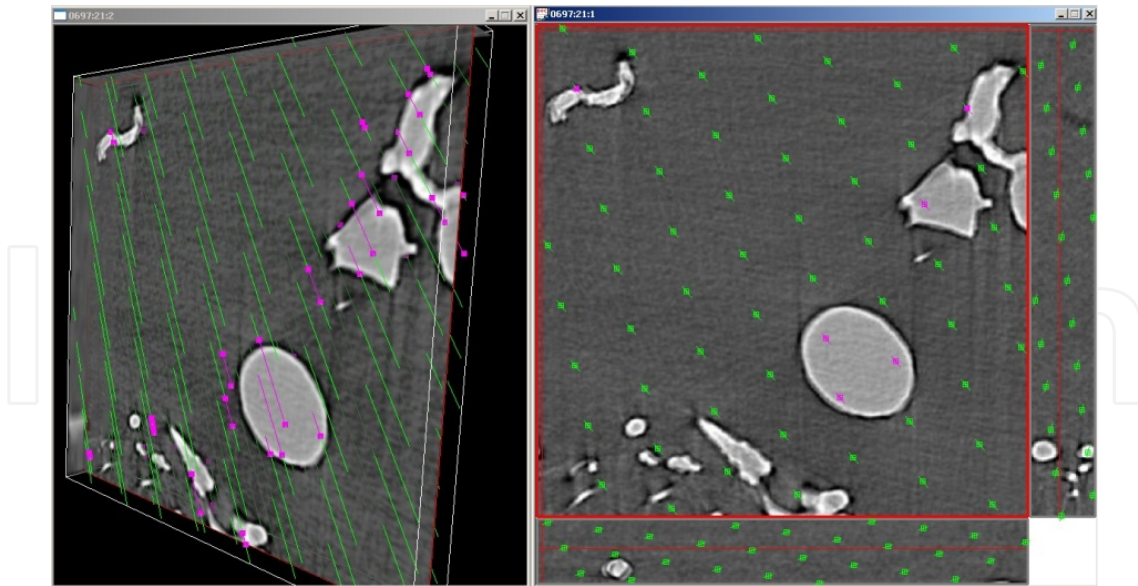
$$S_V = \frac{S}{V(ref)}. \tag{6}$$

Figure 15. Estimating the surface in a series of micro-CT sections with arbitrary orientation using an isotropic triple spatial grid of orthogonal lines with a random initial orientation (fakir probe). The test lines of the fakir probe are green. The violet points denote intersections between the test lines and the current section. The left window shows a 3-D view, the right window shows the current section. Only one third of the triple line system is shown (software Ellipse).

8. Conclusion

This chapter reviews the current approaches in micro-CT imaging and the quantitative evaluation of the resulting image data sets. Both automatic image processing methods and interactive stereological methods are applied for the quantification of the volume fraction, surface density, length density, numerical density, orientation and anisotropy. Micro-CT imaging of bone tissue, tissue-engineered bone scaffolds, and microvascular corrosion casts is quantified using unbiased methods that are already acknowledged in quantitative histology.

Author details

Tomáš Gregor
New Technologies - Research centre, University of West Bohemia, Pilsen, Czech Republic

Petra Kochová
Department of Mechanics, Faculty of Applied Sciences, University of West Bohemia, Pilsen, Czech Republic

Lada Eberlová
Department of Anatomy, Faculty of Medicine in Pilsen, Charles University in Prague, Pilsen, Czech Republic

Lukáš Nedorost, Anna Králíčková and Milena Králíčková
Department of Histology and Embryology, Faculty of Medicine in Pilsen, Charles University in Prague, Pilsen, Czech Republic

Eva Prosecká
Laboratory of Tissue Engineering, Institute of Experimental Medicine, Academy of Sciences of the Czech Republic, v.v.i., Prague, Czech Republic
Institute of Biophysics, Charles University in Prague, Prague, Czech Republic

Václav Liška
Department of Surgery, Charles University Prague, University Hospital in Pilsen, Pilsen, Czech Republic

Hynek Mírka
Department of Imaging Methods, Faculty of Medicine in Pilsen, Charles University in Prague, Faculty Hospital in Pilsen, Pilsen, Czech Republic

David Kachlík
Department of Anatomy, Third Faculty of Medicine, Charles University in Prague, Prague, Czech Republic

Ivan Pirner and Petr Zimmermann
Department of Cybernetics, Faculty of Applied Sciences, University of West Bohemia, Pilsen, Czech Republic

Zbyněk Tonar
European Centre of Excellence NTIS - New Technologies for Information Society, Faculty of Applied Sciences, University of West Bohemia in Pilsen, Pilsen, Czech Republic

Acknowledgement

9. References

Badea, C. T.; Fubara, B.; Hedlund, L.W.; Johnson G. A. (2005). 4-D micro-CT of the mouse heart. *Mol. Imaging*, Vol. 4, pp. 110-116., ISSN 1535-3508.

Bag, S. ; Schambach, S.J. ; Boll, H. ; Schilling, L. ; Groden, C. ; Brochmann, M.A. (2010). Aktueller Stand der Mikro-CT in der experimentellen Kleintierbildgebung. *Fortschr. Roentgestr.*, Vol. 182, pp. 390-403, ISSN 1438-9029.

Bartel, H.; Lametschwandtner, A. (2000). Intussusceptive microvascular growth in the lung of larval Xenopus laevis Daudin: a light microscope, transmission electron microscope and SEM study of microvascular corrosion casts. *Anat. Embryol. (Berl).*, Vol. 202, pp. 55-65, ISSN 0340-2061.

Bentley, M.D.; Ortiz, M.C.; Ritman, E.L.; Romero, C. (2002). The use of Microcomputed tomography to study microvasculature in small rodents. *Am. J. Physiol.—Reg. Integ. Comp. Physiol.*, Vol. 282, pp. 1267–1279, ISSN 0363-6119.

Boll, H.; Nittka, S.; Doyon, F.; Neumaier, M.; Marx, A.; Kramer, M.; Groden, C.; Brockmann, M.A. (2011). Micro-CT based experimental liver imaging using a nanoparticulate contrast agent: a longitudinal study in mice. *PLoS One*, Vol. 6, e25692. ISSN 1932-6203.

Burghardt, A.J.; Link, T.M.; Majumar, S. (2011). High-resolution computed tomography for clinical paging of bone microstructure. *Clin. Orthop. Relat. Res.*, Vol. 469, pp. 2179-2193, ISSN 0009-921X.

Cancedda, R.; Cedola, A.; Giuliani, A.; Komlev, V.; Lagomarsino, S.; Mastrogiacomo, M.; Peyrin, F.; Rustichelli, F. (2007). Bulk and interface investigations of scaffolds and tissue-engineered bones by X-ray microtomography and X-ray microdiffraction. *Biomaterials*, Vol. 28, pp. 2505-2524, ISSN 0142-9612.

Dorsey, S.M.; Lin-Gibson, S.; Simon, C.G. Jr. (2009). X-ray microcomputed tomography for the measurement of cell adhesion and proliferation in polymer scaffolds. *Biomaterials*, Vol. 30, pp. 2967-2974, ISSN 0142-9612.

Fraser, G.M.; Milkovich, S.; Goldman, D.; Ellis, C.G. (2012). Mapping 3-D functional capillary geometry in rat skeletal muscle in vivo. Am. J. Physiol. Heart. Circ. Physiol., Vol. 302, pp. H654-664, ISSN 0363-6135.

Fujisaka, M.; Ohtani, O.; Watanabe, Y. (1996). Distribution of lymphatics in human palatine tonsils: a study by enzyme-histochemistry and scanning electron microscopy of lymphatic corrosion casts. *Arch. Histol. Cytol.*, Vol. 59, pp. 273-280, ISSN 0914-9465.

Gadžijev, E.M.; Ravnik, D. (1996). *Atlas of Applied Internal Liver Anatomy.* Springer, ISBN 978-3211827932, Wien.

Giuvărăşteanu, I. (2007). Scanning electron microscopy of vascular corrosion casts-standard method for studying microvessels. *Rom. J. Morphol. Embryol.*, Vol. 48, pp. 257-261, ISSN 0377-5038.

Gössl, M.; Rosol, M.; Malyar, N.M.; Fitzpatrick, L.A.; Beighley, P.E.; Zamir, M.; Ritman, E.L. (2003). Functional anatomy and hemodynamic characteristics of vasa vasorum in the walls of porcine coronary arteries. *Anat Rec A Discov Mol Cell Evol Biol.*, Vol. 272, pp. 526-537, ISSN 1552-4884.

Gundersen, H.J.; Jensen, E.B. (1987). The efficiency of systematic sampling in stereology and its prediction. *J. Microsc.*, Vol. 147, pp 229-263, ISSN 0022-2720.

Hajnis, K. (1988). The capacity of the sphenoid sinus. *Anat. Anz.*, Vol. 167, pp. 23-28, ISSN 0003-7786.

Havránková, J.; Skoda, V.; Holusa, R. (1989). The use of the Dentacryl rapid (Spofa) resin for preparation of the rat tracheobronchial casts. *Z. Versuchstierkd.*, Vol. 32, pp. 97-100, ISSN 0044-3697.

Ho, S.T.; Hutmacher, D.W. (2006). A comparison of micro CT with other techniques used in the characterization of scaffolds. *Biomaterials Vol.* 27, pp. 1362–1376, ISSN 0142-9612.

Hojo, T. (1993). Scanning electron microscopy of styrene-methylethylketone casts of the airway and the arterial system of the lung. *Scanning Microsc.*, Vol. 7, pp. 287-293, ISSN 0891-7035.

Howard, C.V.; Reed, M.G. (2005). *Unbiased Stereology: Three Dimensional Measurement in Microscopy,* (2nd edition), Garland Science/BIOS Scientific, ISBN 978-1859960899, New York.

Jorgensen, S.M.; Demirkaya, O.; Ritman, E.L. (1998). Three-dimensional imaging of vasculature and parenchyma in intact rodent organs with X-ray micro-CT. *Am. J. Physiol.*, Vol. 275, pp. H1103–1114, ISSN 0002-9513.

Kachlik, D.; Baca, V. (2006). Macroscopic and microscopic intermesenteric communications. *Biomed. Pap. Med. Fac. Univ. Palacky Olomouc Czech Repub.*, Vol. 150, pp. 121-124, ISSN 1213-8118.

Kachlík, D.; Hoch, J. (2008). *The blood supply of the large intestine.* Karolinum, pp. 68-71, ISBN 978-80-246-1397-0, Prague.

Kochová, P.; Cimrman, R.; Janáček, J.; Witter, K.; Tonar, Z. (2011). How to asses, visualize and compare the anisotropy of linear structures reconstructed from optical sections--a study based on histopathological quantification of human brain microvessels. *J. Theor. Biol.*, Vol. 286, pp. 67-78, ISSN 0022-5193.

Kubínová, L.; Janáček, J. (1998). Estimating surface area by the isotropic fakir method from thick slices cut in an arbitrary direction. *J Microsc.*, Vol. 191, pp. 201-211. ISSN 1365-2818.

Kubínová, L.; Janáček, J. (2001). Confocal microscopy and stereology: estimating volume, number, surface area and length by virtual test probes applied to three-dimensional images. *Microsc. Res. Techn.* Vol. 53, pp. 425-435. ISSN 1097-0029.

Lametschwandtner, A.; Minnich, B.; Kachlik, D.; Setina, M.; Stingl, J. (2004). Three-dimensional arrangement of the vasa vasorum in explanted segments of the aged human great saphenous vein: scanning electron microscopy and three-dimensional morphometry of vascular corrosion casts. *Anat. Rec. A Discov. Mol. Cell. Evol. Biol.*, Vol. 281, pp. 1372-1382, ISSN 1552-4884.

Lametschwandtner, A.; Minnich, B.; Stöttinger, B.; Krautgartner, W.D. (2005). Analysis of microvascular trees by means of scanning electron microscopy of vascular casts and 3D-morphometry. *Ital. J. Anat. Embryol.*, Vol. 110, pp. 87-95, ISSN 1122-6714.

Larsen, J.O.; Gundersen, H.J.; Nielsen, J. (1998). Global spatial sampling with isotropic virtual planes: estimators of length density and total length in thick, arbitrarily oriented sections. *J. Microsc.*, Vol. 191, pp. 238-248 ISSN 1365-2818.

Lee, T.C.; Kashyap, R. L.; Chu C.N. (1994). Building skeleton models via 3-D medial surface/axis thinning algorithms.*Graph. Model. Image Process.*, Vol. 56, No. 6, pp. 462-478, ISSN 1077-3169.

Lokkegaard, A.; Nyengaard, J.R.; West, M.J. (2001). Stereological estimates of number and length of capillaries in subdivisions of the human hippocampal region. *Hippocampus*, Vol. 11, pp. 726-740, ISSN 1050-9631.

Ma, X.; Tian, J.; Yang, X.; Qin, C. (2011): Molecular paging in tumor angiogenesis and relevant drug research. *Int. J. of Biomedical Imaging*, Vol. 2011, 370701. ISSN 1687-4196.

Marques-Sampaio, B.P.; Pereira-Sampaio, M.A.; Henry, R.W.; Favorito, L.A.; Sampaio, F.J. (2007). Dog kidney: anatomical relationships between intrarenal arteries and kidney collecting system. *Anat Rec. (Hoboken)*, Vol. 290, pp. 1017-1022, ISSN 1932-8486.

Marsen, M.; Paget, C.; Yu, X.; Henkelman, R.M. (2006). Estimating perfusion using micro-CT to locate microspheres. *Phys. Med. Biol.*, Vol. 51, pp. N9-16, ISSN 0031-9155.

Mather, M.L.; Morgan, S.P.; Crowe, J.A. (2007). Meeting the needs of monitoring in tissue engineering. *Regen. Med.*, Vol. 2, pp. 145–160, ISSN 1746-0751.

Mather, M.L.; Morgan, S.P.; White, L.J.; Tai, H.; Kockenberger, W.; Howdle, S.M. (2008). Image-based characterization of foamed polymeric tissue scaffolds. *Biomed. Mater.*, Vol. 3, pp. 015011 (11pp), ISSN 0955-7717.

Minnich, B.; Bartel, H.; Lametschwandtner, A. (2002). How a highly complex three-dimensional network of blood vessels regresses: the gill blood vascular system of tadpoles of Xenopus during metamorphosis. A SEM study on microvascular corrosion casts. *Microvasc Res.*, Vol. 64, pp. 425-437, ISSN 0026-2862.

Missbach-Guentner, J.; Hunia, J.; Alves, F. (2011). Tumor blood vessel visualization. *Int. J. Dev. Biol.*, Vol. 55, pp. 535-546, ISSN 1696-3547.

Morris, D.E.; Mather, M.L.; Crowe, J.A. (2009). Generation and simulated imaging of pseudo-scaffolds to aid characterisation by X-ray micro CT. *Biomaterials*, Vol. 30, pp. 4233–4246, ISSN 0142-9612.

Mouton, P.R. (2002). *Principles and Practices of Unbiased Stereology. An Introduction for Bioscientists*, The Johns Hopkins University Press, ISBN 0-8018-6797-5, Baltimore.

Müller, R. (1994). Non-invasive bone biopsy: a new method to analyse and display the 3D structure of trabecular bone. *Phys. Med. Biol.*, Vol. 39, pp. 145–164, ISSN 0031-9155.

Müller, R.; Hildebrand, T.; Hauselmann, H.J.; Rüegsegger, P. (1996). Resolution dependency of microstructural properties of cancellous bone based on 3d-microct. *Technol. Health Care*, Vol. 4, pp. 113–119, ISSN 0928-7329.

Müller, R.; van Campenhout, H.; van Damme, B.; van der Perre, G.; Dequeker, J.; Hildebrand, T.; Rüegsegger, P. (1998). Morphometric analysis of human bone biopsies: a quantitative structural comparison of histological sections and micro-computed tomography. *Bone*, Vol. 23, pp. 59–66, ISSN 8756-3282.

Müller, R. (2009). Hierarchical microimaging of bone structure and function. *Nat. Rev. Rheumatol.*, Vol. 5, pp. 373-381, ISSN 1759-4790.

Paluzzi, A.; Belli, A.; Bain, P.; Viva, L. (2007). Brain 'imaging' in the Renaissance. *J. R. Soc. Med.*, Vol. 100, pp. 540-543, ISSN 0141-0768.

Peyrin, F. (2011). Evaluation of bone scaffolds by micro-CT. *Osteoporos. Int.*, Vol. 20, pp. 2043-2048, ISSN 0937-941X.

Prosecká, E.; Rampichová, M.; Vojtová, L.; Tvrdík, D.; Melčáková, Š.; Juhasová, J.; Plencner, M.; Jakubová, R.; Jančář, J.; Nečas, A.; Kochová, P.; Klepáček, K.; Tonar, Z.; Amler, Z. (2011). Optimized conditions for mesenchymal stem cells to differentiate into osteoblasts on a collagen/hydroxyapatite matrix. *J. Biomed. Mater. Res. A*, Vol. 99A, pp. 307-315, ISSN 1552-4965.

Razavi, H.; Dusch M.N.; Zarafshar, S.Y.; Taylor, C.A.; Feinstein, J.A. (2012). A method for quantitative characterization of growth in 3-D structure of rat pulmonary arteries. *Microvasc. Res.*, Vol. 83, pp. 146-153, ISSN 0026-2862.

Renghini, C.; Komlev, V.; Fiori, F.; Verné, E.; Baino, F.; Vitale-Brovarone, C. (2009). Micro-CT studies on 3-D bioactive glass-ceramic scaffolds for bone regeneration. *Acta Biomater.*, Vol. 5, pp. 1328-1337, ISSN 1742-7061.

Ritman, E.L. (2011). Current status of developments and application of micro-CT. *Annu. Rev. Biomed. Eng.*, Vol. 13, pp. 531-552, ISSN 1523-9829.

Roth, H.; Neubrand, T.; Mayer, T. (2010). Improved inspection of miniaturised interconnections by digital X-ray inspection and computed tomography, *Proceedings of Electronics Packaging Technology Conference (EPTC)*, ISBN 978-1-4244-8560-4, Singapore, December 2010.

Rüegsegger, P. (2001). Imaging of bone structure, In: *Bone Mechanics Handbook,* 2nd ed., Cowin S.C. (Ed.), pp.9/1-9/24, CRC Press, ISBN 978-0849391170, Boca Raton.

Savai, R.; Langheinrich, A.C.; Schermuly, R.T.; Pullamsetti, S.S.; Dumitrascu, R.; Traupe, H.; Rau, W.S.; Seeger, W.; Grimminger, F.; Banat, G.A. (2009). Evaluation of angiogenesis using micro-computed tomography in a xenograft mouse model of lung cancer. *Neoplasia*, Vol. 11, pp. 48-56, ISSN 1522-8002.

Schambach, S.J.; Bag, S.; Schilling, L.; Groden, Ch.; Brockmann, M.A. (2010). Application of micro-CT in small animal paging. *Methods*, Vol. 50, pp. 2-13 ISSN 1046-2023.

Schladitz, K. (2011). Quantitative micro-Ct. *J. Microscopy*, Vol. 243, pp. 111-117, ISSN 1365-2818.

Sonka, M.; Hlavac, V.; Boyle, R. (1998). Image processing, Analysis, and Machine Vision. *PWS Publishing,* pp. 123-134, 232-235, ISBN 0-534-95393-X.

Sterio, D.C. (1984). The unbiased estimation of number and sizes of arbitrary particles using the disector. *J. Microsc.*, Vol. 134, pp. 127–136, ISSN 1365-2818.

Tjia, J.S., Moghe, P.V. (1998). Analysis of 3-D microstructure of porous poly(lactide-glycolide) matrices using confocal microscopy. *J. Biomed. Mater. Res.*, Vol. 43, pp. 291–299, ISSN 1552-4965.

Tonar, Z.; Khadang, I.; Fiala, P.; Nedorost, L.; Kochová, P. (2011). Quantification of compact bone microporosities in the basal and alveolar portions of the human mandible using osteocyte lacunar density and area fraction of vascular canals. *Ann Anat.*, Vol. 193, pp. 211-219, ISSN 0940-9602.

Villa, C.; Erratico, S.; Razini, P.; Fiori, F.; Rustichelli, F.; Torrente, Y.; Belicchi, M. (2010). Stem cell tracking by nanotechnologies. *Int J. Mol. Sci.*, Vol. 11, pp. 1070-1081, ISSN 1422-0067.

Zagorchev, L.; Oses, P.; Zhuang, Z.; Moodie, K.; Mulligan-Kehoe, M.J.; Simons, M.; Couffinhal, T. (2010). Micro computed tomography for vascular exploration. *J. Angiogen. Res.*, Vol. 2, pp 7-18, e-ISSN 2040-2384